SAND2022-15030C

Mesoscale Simulations of Pressure-Shear Loading of a Granular Ceramic

Brian J. Demaske[1, a)]

[1]*Sandia National Laboratories, 7011 East Ave., Livermore, CA 94550, USA.*

[a)]Corresponding author: bjdemas@sandia.gov

Abstract. Numerical simulations of pressure-shear loading of a granular ceramic are performed using the shock physics code CTH. A simple mesoscale model for the granular material is used that consists of a randomly packed arrangement of solid spherical grains of uniform size separated by vacuum. The grain material is described by a simple shock equation of state, elastic perfectly plastic strength model, and fracture model with baseline parameters for WC taken from previous mesoscale modeling work. Simulations using the baseline material parameters are performed at the same initial conditions as pressure-shear experiments on dry WC powders. Except for some localized flow regions appearing in simulations with an approximate treatment of sliding interfaces among grains, the samples respond elastically during shear, which contrasts with experimental observations. By extending the simulations to higher shear wave amplitudes, macroscopic shear failure of the simulated samples is observed in simulations with intergranular sliding with the shear strength increasing with increasing stress confinement. At low stress confinement, the shear strength is found to be strongly dependent on the fracture strength of the grains with the shear strength decreasing with decreasing fracture strength. Preliminary simulations indicate worsening agreement with experiment at higher stress confinements even when treating the fracture strength as a variable parameter.

INTRODUCTION

Granular ceramic materials are common in nature and have important applications in planetary science, i.e., terrestrial impact events [1,2], and in the performance of modern armor systems [3], where the failed region ahead of the penetrator is thought to be in a granular or comminuted state [4,5]. As such, it is important to understand how these materials fail at high strain rates. Normal plate impact experiments have been used to characterize the dynamic compaction response of granular ceramics [6-13], however these types of experiments do not provide shear stress information needed for developing constitutive models. Pressure-shear or oblique plate impact experiments, where the projectile nose and target are inclined at some angle relative to the projectile velocity, generate both normal and shear waves in the target simultaneously and can thus be used to directly probe the dynamic shear strength. Such experiments are difficult to perform on granular ceramics and only a handful of materials have been studied to date, including sand (SiO_2) [15,16], tungsten carbide (WC) [16], alumina (Al_2O_3) [17], and boron carbide (B_4C) [18].

Mesoscale models of granular materials have been used in hydrocodes to simulate the dynamic compaction behavior of powders for several decades. The first studies focused on metal powders [19-23] or metal-matrix composites [24] and several years later the same methodology was applied to ceramic powders [25-30]. Despite the brittle nature of ceramics, predictions from mesoscale simulations of normal shock loading were shown to agree well with experimental shock Hugoniot and shock wave rise time data in the form of a similar power-law exponent in Hugoniot stress versus strain rate. Motivated by the success of the previous work, the goal of this work is to conduct mesoscale simulations of pressure-shear loading of a granular ceramic material to see whether this methodology can be used to accurately predict the dynamic shear strength behavior of these materials. A previous study looking at the pressure-shear response of sand [15] presented results of 3D mesoscale simulations in conjunction with experiments, but there was not conclusive evidence of the mesoscale powder model failing macroscopically under shear. In this

work, WC is used as a prototypical ceramic material in the mesoscale simulations as there is data from previous pressure-shear experiments [16] against which to compare simulation results.

SIMULATION DETAILS

Simulations are carried out using the multi-material shock physics code CTH [6]. The computational domain is made up of a Ti-6Al-4V flyer and layered target, which consists of the mesoscale model for granular WC sandwiched between two Ti-6Al-4V anvils. The flyer and target are in intimate contact and at time zero the flyer is given an initial velocity $u_0 = V \cdot \cos\theta$ along the x-axis and $v_0 = V \cdot \sin\theta$ along the y-axis, where V and θ correspond to the magnitude of the flyer velocity and nose angle, respectively. Boundaries along the x-axis are free and periodic boundaries are maintained along the transverse directions. The anvil thicknesses are 8 mm to coincide with those in experiment [16], while the flyer thickness is set to 12 mm to prevent release waves originating from the flyer free surface from reaching the granular WC layer prior to the release waves originating from the rear anvil free surface. The granular WC layer is modeled as a collection of randomly packed, spherical grains separated by vacuum. All grains have a diameter of 25 μm, which lies within the range of grain sizes in experiment (=20-32 μm). The sample thickness is 0.25 mm to match experiment, while the cross-section is 0.5x0.25 mm, which corresponds to the same dimensions (normalized by the grain diameter) used in previous mesoscale pressure-shear simulations on sand [15]. Initial densities of the samples used in experiment were not measured, so the model assumes an initial porosity of 35% yielding a total of 2483 grains in the granular WC layer. An illustration of the computational domain is shown in Fig. 1.

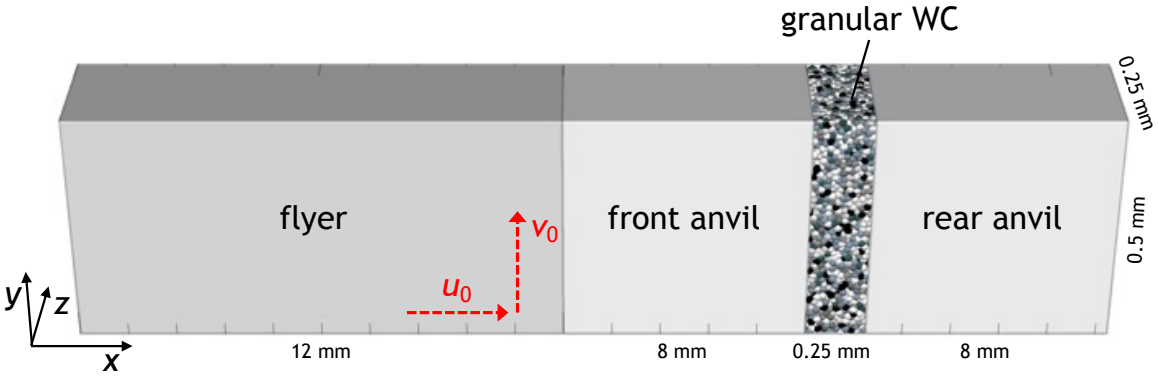

FIGURE 1. An illustration of the computational domain used in the pressure-shear simulations. The thicknesses of the flyer and anvils are greatly reduced to aid in visualization of the granular WC layer.

The flyer and anvils are both treated as homogeneous elastic materials with mechanical properties chosen to match the longitudinal and transverse sound speeds for Ti-6Al-4V measured in experiment [31]. The WC grains are treated using a Mie-Grüneisen equation of state (EOS) and an elastic perfectly plastic strength model with a cap on the tensile pressure to model fracture. The choice of simple material models for WC is motivated by previous mesoscale simulations of shock compaction of granular WC [27,28,30]. Baseline parameter values for the material models are given in Table 1. By default in CTH, all materials that reside in a single computational cell share a common velocity and materials become welded together at interfaces. An alternate treatment is to set the shear velocity gradients in mixed-material cells to zero, which leads to approximate sliding behavior at material interfaces. Simulations with both mixed-material cell treatments applied to the WC grains are performed to examine the effect on the response. A plane of Lagrangian tracer particles distributed near the rear anvil free surface is used to record the average velocity of this interface to allow for direct comparison with Photon Doppler velocimetry (PDV) data collected in experiment [16]. An adaptive mesh refinement scheme is devised to limit high-resolution mesh (cell size of ~2 μm) to the granular WC layer, while a much coarser mesh (cell size of ~8 μm) is allocated to all other regions.

TABLE 1. Parameters for material models used in the pressure-shear simulations. Parameters for WC are taken from Ref. [27], while the bulk sound speed c_0, initial density ρ_0, and Poisson ratio ν for Ti-6Al-4V are chosen to ensure the simulations give the same longitudinal and transverse sound speeds as measured in experiment [31].

Parameter	WC	Ti-6Al-4V
Initial density, ρ_0 (g cm^{-3})	15.56	4.415
Bulk sound speed, c_0 (km s^{-1})	5.26	4.91
Hugoniot slope, S	1.15	-
Gruneisen parameter, Γ	1.0	-
Specific heat, C_V (J kg^{-1} K^{-1})	172	-
Yield stress, Y_0 (GPa)	5	-
Poisson ratio, ν	0.2	0.317
Fracture strength, σ_f (GPa)	4	-

SIMULATION RESULTS

Two sets of 3D mesoscale simulations using the baseline parameter sets in Table 1 are performed for the same initial impact conditions as in experiment: $\theta = 20°$ and $V = 66$, 121, and 145 m/s. The first set uses the default welded treatment of WC grains, while the second set uses the approximate slide treatment. Normal and transverse velocity histories for the target's rear surface for both sets of simulations are shown in Fig. 2 along with experimental data. Time is shifted such that zero corresponds to the arrival of the normal wave at the rear surface. The shear arrives ~2.3 μs later. Simulations with the welded grain behavior exhibit a rapid increase in the normal velocity to the expected level u_0 corresponding to much less compaction than observed in experiment. With intergranular sliding enabled, the normal velocity rise becomes more gradual indicating more compaction that is in better agreement with experiment. However, the slide simulations still overpredict the height of the initial shoulder of the normal velocity rise relative to experiment. For the lowest impact velocity case ($V = 66$ m/s), the normal velocity remains at a nearly constant level $< u_0$ then jumps up to near u_0 after ~2 μs, whereas in experiment the approach to u_0 is much more gradual.

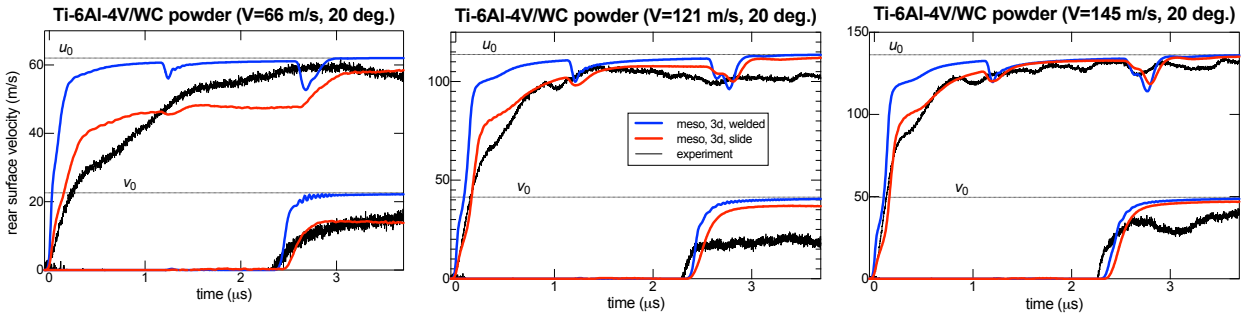

FIGURE 2. Normal and transverse rear surface velocity histories from the current mesoscale simulations and previous pressure-shear experiments on granular WC [16].

Transverse velocity histories for simulations with the default welded grain interfaces show a smooth rise to the expected level v_0 for all three impact velocities. Visual inspection of the simulated granular WC layer during and after loading by the shear wave indicates some grain deformation and rearrangement during the shear wave rise, but afterwards the grains reach a stable configuration in which no further macroscopic shear flow occurs. Since v_0 represents the input transverse velocity from the front anvil, then the simulated granular WC layer with the welded grain behavior is responding elastically to the shear loading. By contrast, the samples in experiment do not reach v_0 and so are failing under the same shear load. Enforcing the slide condition for the grains leads to a reduction in the transverse velocity level after rise to below v_0 and the reduction becomes more pronounced with decreasing impact velocity. Despite the reduction in the transmitted transverse velocity, visual inspection of the WC grains during shear loading indicate similar behavior to the welded grain simulations in that no macroscopic shear flow occurs once the grains reach a stable configuration after the initial shear wave rise. The difference in response seems to originate from localized flow at grain interfaces in the slide simulations that is exacerbated at low velocities.

To probe the shear failure surface of the mesoscale powder model, sets of simulations are performed fixing the normal confinement stress σ_{el} at three different levels and increasing the shear wave amplitude τ_{el} from 1-2 GPa. The values for σ_{el} chosen are 0.838, 1.842, and 4 GPa; the first two values correspond to experiments at impact velocities of 66 and 145 m/s and the last corresponds to the fracture strength σ_f of the modeled WC material. Simulations with the welded grain behavior respond elastically to the shear loading up to the maximum shear wave amplitude for all values of σ_{el}, whereas simulations with intergranular sliding exhibit an upper bound in the transmitted transverse velocity that is less than the maximum shear wave amplitude. Transverse velocity histories for simulations with intergranular sliding are plotted in Fig. 4(a). Transverse velocity histories for σ_{el} = 0.838 GPa exhibit a clear upper bound in the velocity transmitted by the granular WC layer that is far below the expected level for an elastic response. Visual inspection of the WC grains shows grains rearranging and deforming throughout the loading by the shear wave. At higher values of τ_{el}, a line-like shear interface forms inside the granular WC layer, which can no longer effectively transmit transverse velocity from one side to the other, see Fig. 4(b). This manifests as a peak in the transverse velocity history followed by a decrease. Increasing the stress confinement leads to an increase in the upper bound in the transmitted transverse velocity, which corresponds to an increase in the shear strength as is typical of granular materials. At the highest stress confinement (σ_{el} = 4 GPa), there is a sharp transition between the granular WC layer fully transmitting the input shear wave and formation of an internal shear interface.

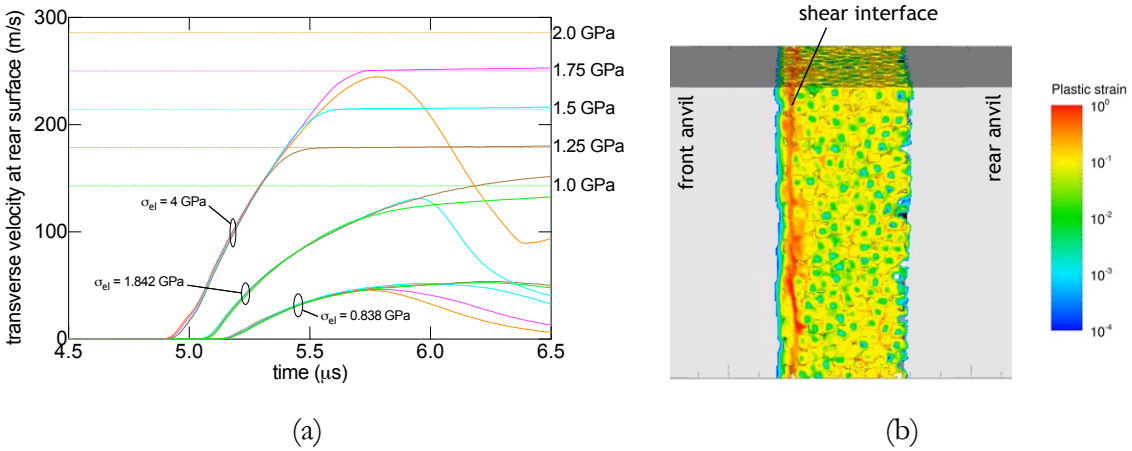

FIGURE 4. (a) Transverse rear surface velocity histories from mesoscale simulations with intergranular sliding. The color of each curve corresponds to the amplitude of the input shear wave τ_{el} and group of curves are labeled according to the normal wave amplitude σ_{el}. Horizontal lines indicate the rear surface transverse velocity for a given value of τ_{el} in the absence of the granular WC layer. (b) Snapshot of plastic strain showing the formation of a line-like shear interface within the granular WC layer.

Post-recovery microscopy images of granular WC samples in experiment show significant evidence of grain fracture [16], while simulations at the shear failure surface show very few cells containing WC reach tensile pressures close to the baseline fracture strength σ_f. To examine the effect of the fracture strength of WC on the pressure-shear response, the fracture criterion is changed from tensile pressure to maximum principal stress and σ_f is varied from its baseline value of 4 GPa down to 10^{-9} GPa. Normal and transverse velocity histories for these simulations are shown in Fig. 5, where each curve is calculated by taking the upper bound in the simulation data for several runs varying τ_{el} over the range 0.25-2 GPa. The normal wave amplitude σ_{el} = 0.838 GPa. Normal velocity histories show decreasing σ_f leads to a reduction in the height of the initial shoulder and thus more compaction, which is in better agreement with experiment. For the near-zero-fracture-strength case, a snowplow-like compaction response is observed in which the sample becomes fully compacted behind the normal wave front. Transverse velocity histories show a reduction in the velocity level after rise as σ_f is lowered from 4 GPa to 0.5 GPa, which indicates a decrease in the shear strength of the granular WC layer. For σ_f below 0.25 GPa, the transverse velocity level after rise increases and for the near-zero-fracture-strength case exhibits a nearly constant plateau. Plotting all simulation runs separately for this case would result in a set of curves like those obtained for σ_{el} = 4 GPa in Fig. 4(a), i.e., those characteristic of a sharp transition between fully supporting the input shear wave amplitude to formation of a shear interface within the granular WC layer. However, in the current case, the maximum transverse velocity the granular layer can support before formation of an internal shear interface is much less.

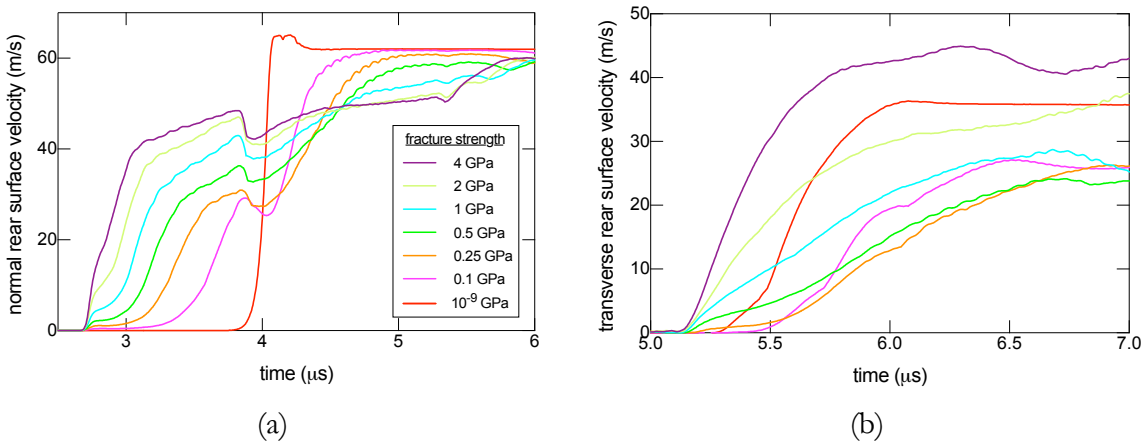

FIGURE 5. (a) Normal and (b) transverse rear surface velocity histories from mesoscale simulations with different values of the fracture strength of the WC grain material.

CONCLUSION

Simulations of pressure-shear loading were presented for a granular ceramic material described by a simple mesoscale model with material models and baseline parameters taken from previous mesoscale simulations of shock compression of granular WC. Simulations were performed at the same initial conditions as in previous pressure-shear experiments on dry granular WC [16] and showed essentially an elastic response to the shear loading in contrast to experimental observations. Simulations with intergranular sliding exhibited reduced transverse velocity levels, which are thought to be attributed to localized flow at grain interfaces that was exacerbated at low impact velocities. By simulating higher shear wave amplitudes than possible in experiment, the mesoscale powder model was observed to fail in simulations with intergranular sliding with the failure behavior characterized by grain rearrangement and deformation and formation of line-like, internal shear interfaces at sufficiently high initial shear wave amplitudes. Lowering the intragranular fracture strength was shown to reduce the shear strength of the simulated powder, but only to a certain point beyond which the shear strength started to increase with increasing fracture strength. By treating the fracture strength as a variable parameter, results of the mesoscale simulations start to approach those of experiment at low stress confinement (~1 GPa). However, preliminary simulations show that this agreement worsens with increasing stress confinement as simulations start to severely overpredict experimental shear strengths. Moreover, it's unclear whether the good agreement at low stress confinement is a byproduct of numerical issues with the slide algorithm. Ultimately, the Eulerian nature of the simulations limits their usefulness for this problem as contact and fracture are not treated realistically. Future work should explore other methods that treat contact more realistically in Eulerian simulations like the extended finite element method or alternate methodologies like Lagrangian finite element simulations or peridynamics.

ACKNOWLEDGMENTS

Sandia National Laboratories is a multimission laboratory managed and operated by National Technology and Engineering Solutions of Sandia, LLC, a wholly owned subsidiary of Honeywell International Inc., for the U.S. Department of Energy's National Nuclear Security Administration under contract DE-NA0003525.

REFERENCES

1. P. Lambert and H Trumel, in *Materials under Extreme Loadings: Applications to Penetration and Impact*, edited by G. Voyiadjis, E. Buzaud and I. R. Ionescu (Wiley, 2010).
2. M. Iskander, S. Bless and M. Omidvar, *Rapid Penetration into Granular Media: Visualizing the Fundamental Physics of Rapid Earth Penetration*, (Elsevier, 2015).
3. W.A. Gooch, Ceramic Transactions **134**, 3-21 (2002).

4. D. A. Shockey, A. H. Marchand, S. R. Skaggs, G. E. Cort, M. W. Burkett and R. Parker, International Journal of Impact Engineering **9** (3), 263-275 (1990).
5. M. A. Meyers, *Dynamic Behavior of Materials*. (Wiley, 1994).
6. T. Akashi, V. Lotrich, A. Sawaoka and E. K. Beauchamp, Journal of the American Ceramic Society **68** (12), 322-324 (1985).
7. K.I. Kondo, S. Soga, A. Sawaoka and M. Araki, Journal of Materials Science **20** (3), 1033-1048 (1985).
8. T. Taniguchi, K. Kondo and A. Sawaoka, Journal of Applied Physics **61** (1), 196-200 (1987).
9. J.A. Akins and T.J. Ahrens, Geophysical Research Letters **29** (10), 31-31-31-34 (2002).
10. J. P. Borg, D. J. Chapman, K. Tsembelis, W. G. Proud and J. R. Cogar, Journal of Applied Physics **98** (7), 073509 (2005).
11. J. L. Brown, T. J. Vogler, D. E. Grady, W. D. Reinhart, L. C. Chhabildas and T. F. Thornhill, AIP Conference Proceedings **955** (1), 1363-1366 (2007).
12. W. G. Proud, D. J. Chapman, D. M. Williamson, K. Tsembelis, J. Addiss, A. Bragov, A. Lomunov, I. G. Cullis, P. D. Church, P. Gould, D. Porter, J. R. Cogar and J. Borg, AIP Conference Proceedings **955** (1), 1403-1408 (2007).
13. T. J. Vogler, M. Y. Lee and D. E. Grady, International Journal of Solids and Structures **44** (2), 636-658 (2007).
14. A. S. Abou-Sayed, R. J. Clifton and L. Hermann, Experimental Mechanics **16** (4), 127-132 (1976).
15. J. W. LaJeunesse, "Dynamic Behavior of Granular Earth Materials Subjected to Pressure-shear Loading", Ph.D. thesis, Marquette University, 2018.
16. W. D. Reinhart, T. F. Thornhill, III, T. J. Vogler and C. S. Alexander, Sandia National Laboratories Report No. SAND2011-6700, 2011 (unpublished).
17. S. Sairam and R. J. Clifton, Brown University Report No. AD-A-296109/2/XAB, 1994 (unpublished).
18. X. Sun, A. Chauhan, D. D. Mallick, A. L. Tonge, J. W. McCauley, K. J. Hemker, J. C. LaSalvia and K. T. Ramesh, Journal of the Mechanics and Physics of Solids **143**, 104031 (2020).
19. R. L. Williamson, Journal of Applied Physics **68** (3), 1287-1296 (1990).
20. D. J. Benson, Modelling and Simulation in Materials Science and Engineering **2** (3A), 535 (1994).
21. D. J. Benson and W. J. Nellis, Applied Physics Letters **65** (4), 418-420 (1994).
22. D. J. Benson, V. F. Nesterenko, F. Jonsdottir and M. A. Meyers, Journal of the Mechanics and Physics of Solids **45** (11), 1955-1999 (1997).
23. M. A. Meyers, D. J. Benson and E. A. Olevsky, Acta Materialia **47** (7), 2089-2108 (1999).
24. D. J. Benson, W. Tong and G. Ravichandran, Modelling and Simulation in Materials Science and Engineering **3** (6), 771 (1995).
25. J. P. Borg and T. J. Vogler, AIP Conference Proceedings **955** (1), 227-230 (2007).
26. T. J. Vogler and J. P. Borg, AIP Conference Proceedings **955** (1), 291-294 (2007).
27. J. P. Borg and T. J. Vogler, International Journal of Solids and Structures **45** (6), 1676-1696 (2008).
28. J. P. Borg and T. J. Vogler, Modelling and Simulation in Materials Science and Engineering **17** (4), 045003 (2009).
29. J. P. Borg, T. J. Vogler and A. Fraser, AIP Conference Proceedings **1195** (1), 1331-1336 (2009).
30. J. P. Borg and T. J. Vogler, Shock Waves **23** (2), 153-176 (2013).
31. D. P. Dandekar and S. V. Spletzer, AIP Conference Proceedings **505** (1), 427-430 (2000).